Materials Science & Engineering A 682 (2017) 238–247

Contents lists available at ScienceDirect

Materials Science & Engineering A

journal homepage: www.elsevier.com/locate/msea

As cast microstructures on the mechanical and corrosion behaviour of ZK40 modified with Gd and Nd additions

R.H. Buzolin[a,b,*], M. Mohedano[a,c], C.L. Mendis[a], B. Mingo[c], D. Tolnai[a], C. Blawert[a], K.U. Kainer[a], H. Pinto[b], N. Hort[a]

[a] Magnesium Innovation Centre, Helmholtz-Zentrum Geesthacht, Max-Planck-Strasse 1, D 21502 Geesthacht, Germany
[b] Department of Materials Engineering, University of Sao Paulo, Av. Joao Dagnone, 1100 Jd. Sta Angelina, 13563-120 Sao Carlos, Brazil
[c] Departamento de Ciencia de Materiales, Facultad de Ciencias Químicas, Universidad Complutense, 28040 Madrid, Spain

ARTICLE INFO

Keywords:
Mg-Zn-Zr alloys
Rare earth additions
Corrosion
Mechanical properties

ABSTRACT

The microstructure of ZK40, ZK40 with 2 wt% of Nd and Gd (ZK40-2Nd and ZK40-2Gd, respectively) were investigated with optical, scanning and transmission electron microscopy, X-ray diffraction and Scanning Kelvin Probe Force Microscopy. The mechanical properties and the corrosion behaviour were correlated with the microstructure. The 2 wt% Gd addition enhanced the ductility, while the Nd addition resulted in deterioration in mechanical properties. The corrosion behaviour was also enhanced with the addition of Gd.

1. Introduction

Mg alloys offer a high potential for use as lightweight structural materials in the automotive and aerospace industry. However, satisfactory mechanical properties are not enough to promote a magnesium alloy for commercial applications where corrosion resistance also plays an important role. In fact, Mg alloys usually have relatively low corrosion resistance, which is one of the main obstacles that impede the use of magnesium alloys [1].

Several approaches have been developed with the aim of enhancing the corrosion resistance of the Mg alloy involving the addition of alloying elements. The AZ Mg alloys have been extensively studied, such as AZ31 due to mainly its promising applications in forming, or AZ91 for high pressure die casting [2]. The influence of the RE elements on the mechanical properties [3] and corrosion behaviour [4,5] of Mg-Al alloy system has also been investigated. In the AZ system the second phases can act as a galvanic cathode and accelerate the corrosion rate of the matrix if the volume fraction of the second phases is small [6,7]. On the other hand, if there is a larger amount of second phase that it forms as a continuous network it may act as an anodic barrier to inhibit the overall corrosion of the alloy.

In the case of Mg-Zn alloys, the effect of addition of rare earth on the corrosion behaviour has yet not been fully understood [8]. Among these investigations, the as cast ZE41 (Mg-Zn-RE alloy) is in the focus of most of the studies. Compared with the AZ alloys, the eutectic phases in ZE41 are reported to not play the role of corrosion barrier retarding the progress of the corrosion [9]. For ZE41 immersed in 1 N NaCl, Zhao et al. [9] showed that the corrosion initiated as localised corrosion. It started at some sites on the surface and expanded over the surface forming a thick layer of corrosion products. Neil et al. [10] reported that segregation of Zr in the α-Mg matrix played a distinct role on the early stages of corrosion in the ZE41. However, among the investigated Mg alloy systems, Mg-Zn-Zr (ZK) alloys are one of the higher strength cast alloys available commercially [11]. The small addition of rare earth (RE) elements to the ZK alloys can alter the microstructure and therefore can modify the mechanical properties and give satisfactory corrosion resistance. It is reported that the addition of rare earth (RE) elements and alkaline metals to Mg alloys improves the corrosion resistance [4,5]. The addition of RE [12] enhanced the castability and elevated temperature strength [13]. The RE additions are grain refiners, attributed mainly to the constitutional supercooling [14], which can lead to improved ductility at room temperature [15,16].

However, the role of individual rare earth elements on the mechanical behaviour and corrosion resistance of ZK series alloys has not been fully investigated. The aim of the present work is to study the influence of Gd and Nd additions on the microstructure, mechanical properties and corrosion behaviour.

2. Experimental procedure

2.1. Materials

Pure Mg, Zn, Nd and master alloys Mg 4 wt% Gd and Mg-33 wt% Zr

* Corresponding author at: Magnesium Innovation Centre, Helmholtz-Zentrum Geesthacht, Max-Planck-Strasse 1, D 21502 Geesthacht, Germany.
E-mail address: ricardo.buzolin@hzg.de (R.H. Buzolin).

http://dx.doi.org/10.1016/j.msea.2016.11.022
Received 23 August 2016; Received in revised form 3 November 2016; Accepted 8 November 2016
Available online 17 November 2016
0921-5093/ © 2016 Elsevier B.V. All rights reserved.

Table 1
Analysed chemical compositions.

Alloys	Zn (wt %)	Zr (wt%)	Gd (wt %)	Nd (wt %)	Fe (ppm)	Cu (ppm)	Ni (ppm)
ZK40	5.00	0.53	–	–	11.3	14.1	12.8
ZK40-2Gd	4.50	0.55	1.70	–	6.9	29.2	<30
ZK40-2Nd	4.70	0.55	–	2.46	11	14.8	28.2

(Zirmax®) were used to prepare the alloys. Mg was molten in an electric resistance furnace under protective atmosphere of Ar with 2 vol% SF_6 and held at 750 °C where alloying additions were added to the melt and stirred for 10 min. The melt was poured into a preheated thin walled steel mould, held at 660 °C for 15 min before immersing into water at a rate of 10 mm s^{-1} until the top of the melt was in line with the cooling water. This indirect chill casting procedure was performed in order to provide a homogeneous microstructure. Zr and Gd were measured with Bruker S5 X-ray fluorescence spectrometer. Zn, Nd, Fe, Cu and Ni were measured with a Spectrolab spark analyser.

2.2. Differential thermal analysis (DTA)

Specimens for Differential Thermal Analysis (DTA) were prepared by placing approximately 30–45 mg of the alloys in Metttler Toledo crucible in an Ar atmosphere. The analysis were performed using a Parkin Elmer DTA machine at a heating and cooling rate of 10 K/min in the temperature range from 300 to 700 °C. Three heating and cooling cycles were used for each alloy to ensure repeatability of the measurement.

2.3. Specimen preparation and characterisation

For metallographic characterisation, specimens were ground through successive grades of silicon carbide abrasive papers from P500 to P2500, followed by polishing with a 3 μm diamond suspension and finally in OPS with 1 μm diamond suspension. The specimens analysed by optical microscopy (OM) were etched with an acetic picric acid solution [17] to reveal the constituents of the alloys. The analyses were performed using a reflected light microscope Leica DMI 5000. Grain size was determined according to the ASTM E112-12 standard using the linear intercepts method. Polished samples were examined with scanning electron microscopy (SEM) using a Zeiss FEG-SEM Ultra 55, a Inspect F50 and a Tescan Vega3 SEM using BSE and SE modes. The SEMs were equipped with Energy dispersive X-ray (EDX) spectrometer. EDX spectra profiles were obtained across the grains to determine the distribution of elements. Savitzky-Golay [18] smooth filter was applied using Origin with 20 points of window to fit a 4-degree polynomial.

Phase characterisation of the as-cast specimens was conducted with synchrotron radiation diffraction (SRD) using the facilities of P07 beamline of Petra III, DESY (*Deutsches Elektronen-Synchrotron*). A monochromatic beam with energy of 100 keV (λ=0.0124 nm) and with a cross-section of 1.0 mm×1.0 mm was used. Diffraction patterns were recorded with a PerkinElmer 1622 flat panel detector with a pixel size of $(200\ \mu m)^2$, which was placed at a sample-to-detector distance of 1535 mm from the specimen (calibrated with a LaB_6 standard powder sample). The Pearson crystallographic database was used to obtain the information of possible phases and CaRIne crystallographic software was used to simulate the theoretical diffraction patterns for various phases.

The samples for transmission electron microscopy (TEM) were prepared by cutting 0.5 mm slices with Struers Isomat precision saw followed by thinning to 150 μm in thickness using 500 grit SiC paper. Then 3 mm diameter discs were punched using a disc punch and electropolished using a Fischione twin jet electropolisher at −45 °C with a voltage of 50 V in solution of 1.5 vol% perchloric acid in ethanol to perforation. TEM analysis was conducted with a FEI CM 200 transmission electron microscope operating at 200 kV equipped with an Oxford EDAX Energy dispersive X-ray spectrometer (EDX) and quantitative composition measured using standardless thin film technique.

Scanning Kelvin Probe Force Microscopy (SKPFM) working in tapping mode was performed using a Nanoscope IIIa MultiMode microscope. Surface potential maps were obtained using a silicon tip with a platinum coating of 20 nm thickness. The topographic and surface potential images were obtained simultaneously and the tip to sample distance was kept constant at 100 nm. The tested samples were metallographically prepared and polished to a 0.25 μm diamond suspension finish. All measurements were performed at room temperature and the relativity humidity was in the range of 40–65%. SEM/EDS analyses were performed in the SKPFM-examined regions to identify the second phases.

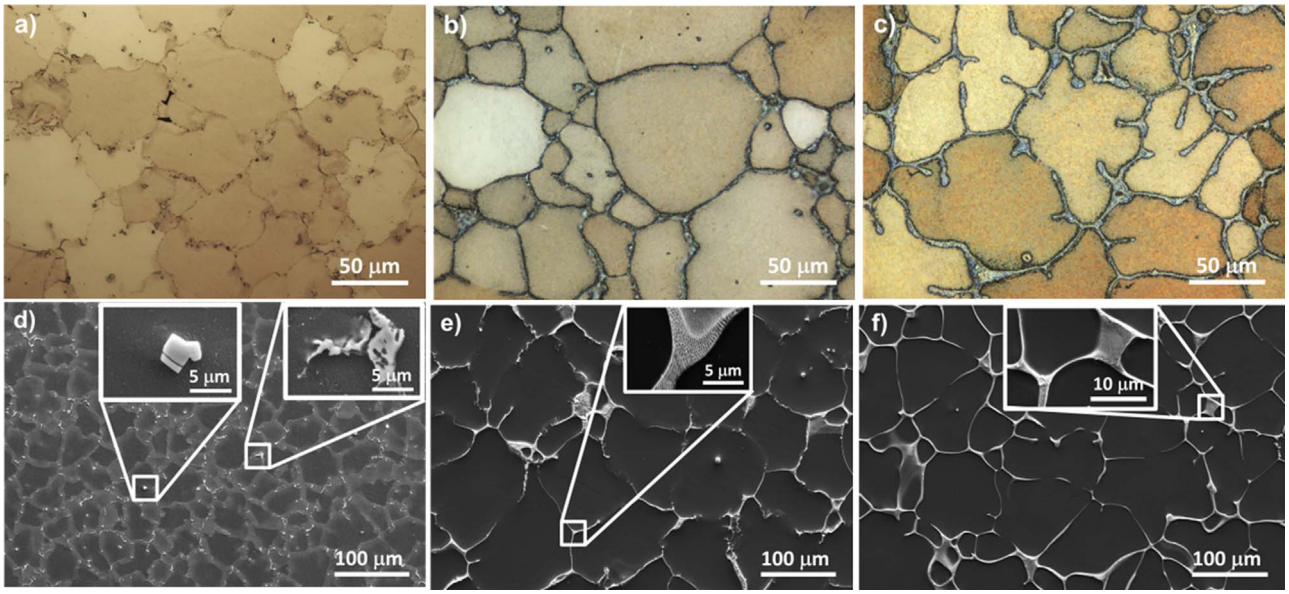

Fig. 1. (a)–(c) Optical micrographs and (d)–(f) SEM micrographs typical of as-cast (a), (d) ZK40; (b), (e) ZK40-2Gd; (c), (f) ZK40-2Nd alloys.

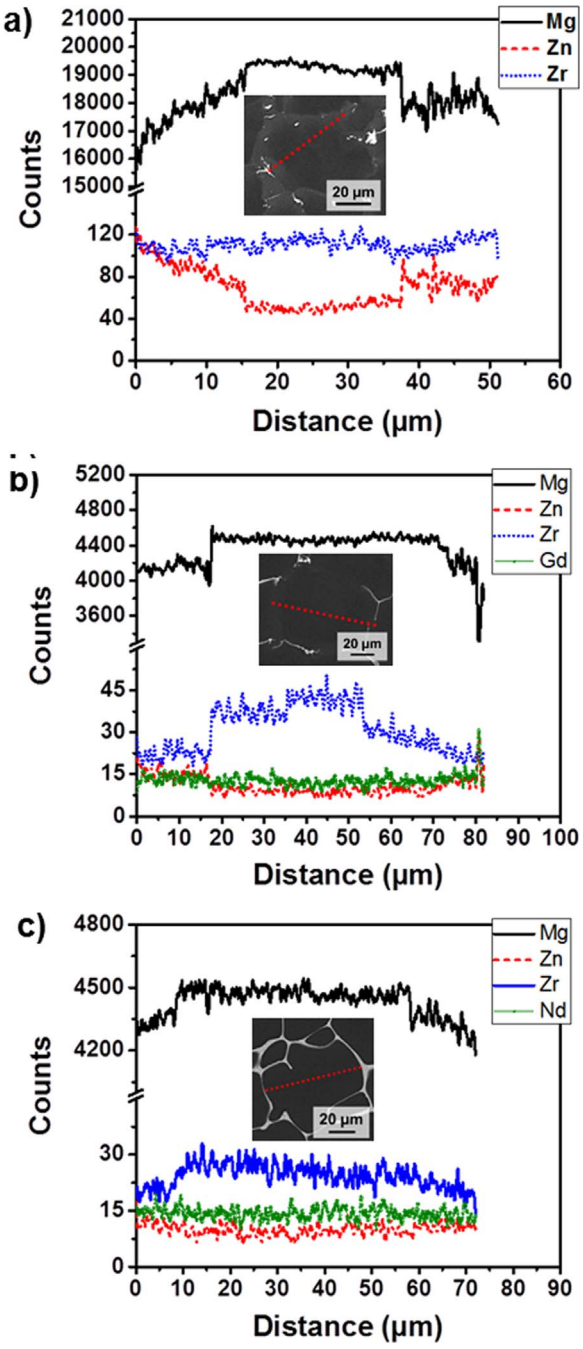

Fig. 2. EDX spectra line profiles for the: (a) ZK40; (b) ZK40-2Gd; (c) ZK40-2Nd across a typical grain.

2.4. Mechanical testing

Cylindrical compression specimens with 10 mm diameter and 15 mm length and tensile specimen with diameter of 6 mm were manufactured according to DIN 50125 (ISO 6892-1) from the as cast ingots. Both tests were performed in a Zwick Z050 mechanical testing machine with a strain rate of 0.001 mm/min at room temperature and five samples were tested per alloy.

2.5. Electrochemical measurements

Electrochemical tests were conducted in a stirred aqueous 0.5 wt% NaCl solution at 22 ± 0.5 °C using a Gill AC computer-controlled potentiostat. A typical three-electrode cell with the specimen as the working electrode (0.5 cm^2 exposed area), a saturated Ag/AgCl electrode as the reference electrode, and a platinum mesh as a counter electrode was used.

Electrochemical impedance spectroscopy (EIS) measurements were performed for immersion times ranging from 1 h to 1 day at room temperature. The frequency range was from 0.01Hz to 30 kHz and the amplitude of the sinusoidal potential signal was 10 mV with respect to the OCP. The impedance spectra were analysed using ZView® software. The errors for the individual parameters of the equivalent electrical circuits (such as CPE and R) were <5% and with values of the goodness of fit of the simulated spectra corresponded to χ^2 <0.01.

2.6. Hydrogen evolution measurements

Details of the procedure, design and the relationship between the volume of hydrogen evolution and the mass loss of the specimen can be found elsewhere [19,20]. Hydrogen evolution measurements were performed in 0.5 wt% NaCl naturally-aerated solution for up to 14 days for ZK40 and ZK40-2Gd alloys and up to 7 days for ZK40-2Nd. After the corrosion tests, specimens were characterised with SEM in order to investigate the morphology and composition of the corrosion products.

2.7. Initial steps of corrosion

Immersion tests were performed for 4 h, 8 h and 24 h in 0.5 wt% NaCl naturally-aerated solution in order to investigate the initiation of corrosion process. The final sample surface was prepared with OPS polishing to ensure that the sample preparation did not contribute to the corrosion process. Finally, the corroded surface was investigated with SEM after the removal of the corrosion products by pickling in a solution containing 200 g/L CrO_3 at room temperature for 5–10 min following the ASTM standard G1-90, Designation C5.2.

3. Results and discussion

3.1. Microstructure

The actual compositions of the alloys are given in Table 1. The optical (a–c) and scanning electron microscopy (d–f) for ZK40 (a,d), ZK40-2Gd (b,e) and ZK40-2Nd (c,f) are shown in Fig. 1. Relatively uniform microstructures were observed for each alloy. ZK40-2Nd exhibits the most pronounced dendritic microstructure, and has a more uniform microstructure compared with other two alloys. The ZK40 had an average grain size of 37.4 ± 2.1 μm, the ZK40-2Gd of 46.1 ± 9.1 μm and the ZK40-2Nd had an average grain size of 67.1 ± 5.4 μm.

The SEM micrographs illustrate the area fraction of intermetallic particles, with ZK40, ZK40-2Gd and ZK40-2Nd alloys contained 1.6 ± 0.5%, 5.7 ± 1.0% and 7.3 ± 0.6% intermetallic particles, respectively. Additionally, in the ZK40 alloy segregation of Zn towards the grain boundary is observed as illustrated by brighter regions along the grain boundary in Fig. 1(d). ZK40-2Gd (Fig. 2(b)) has higher concentration of Zr within the grain. No significant chemical segregation was observed in the ZK40-2Nd alloy (Fig. 2(c)). The Gd and Nd distribute along the grain boundaries in the modified alloys. In the ZK40 alloy, discrete particles of intermetallic phase are observed randomly at triple points and grain boundaries, illustrated by the insert in Fig. 1(d). The ZK40-2Gd and ZK40-2Nd alloys contains a semi-continuous distribution of intermetallic particles along the grain boundaries. Therefore, the as-cast microstructure of the ZK40 alloy was modified with Gd and Nd. The RE containing alloys contained a semi-continuous network of intermetallic particles reinforcing the grain boundary, Fig. 1. Similar microstructure was reported for the ZE41 alloy [9,10].

The EDX spectra shows the segregation of elements in the alloys investigated, Fig. 2. Zn segregates and a concentration was observed near the grain boundary for the ZK40 and ZK40-2Gd alloys. The

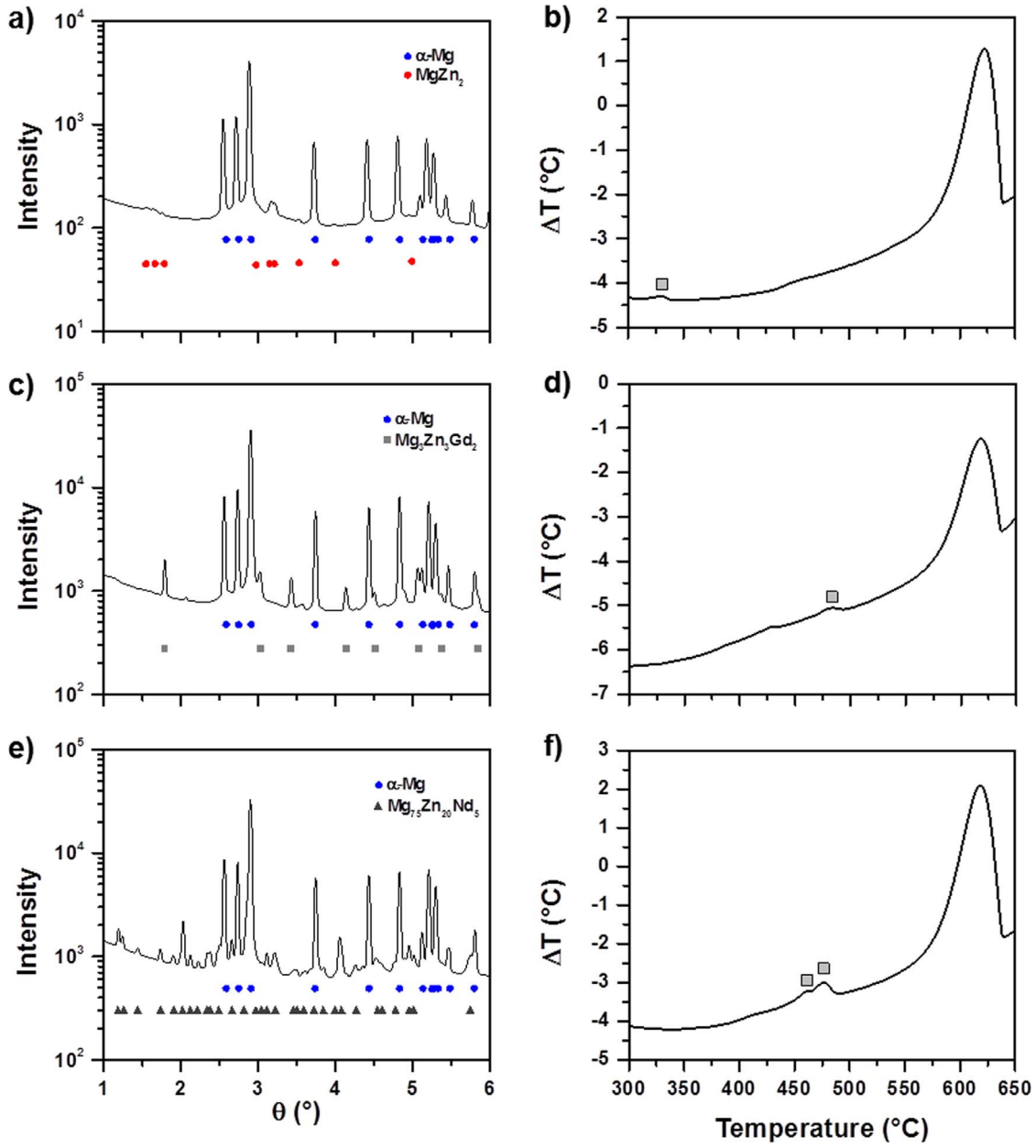

Fig. 3. (a) XRD linescan profiles for the ZK40-2Gd and ZK40-2Nd alloys in the as-cast condition; (b) DTA cooling curves for the ZK40, ZK40-2Gd and ZK40-2Nd alloys.

inverse segregation of Zr is observed for the ZK40-2Gd, while only minor Zr segregation was observed in Nd containing alloy. The RE (Gd and Nd) elements do not seem to segregate within the grain.

The SRD line profiles from all investigated alloys show that they consisted of α-Mg and intermetallic phases, Fig. 3(a), (c), and (e). The intermetallic phase was alloy dependent and the ZK40 alloy contained $MgZn_2$ phase. The ZK40-2Gd contained $(Mg, Zn)_3Gd_2$ intermetallic phase, in addition to α-Mg. Liu et al. [27] reported the presence of the $(Mg, Zn)_3Gd_2$ for a Mg-4.58Zn-2Gd-0.18Zr alloy. Due to the large number of peaks observed in the SRD line profile of the ZK40-2Nd alloy, the intermetallic particles were analysed with TEM to confirm the intermetallic phases, Fig. 4. The composition of the phase was 71.8 ± 7.2 at% Mg 20.3 ± 5.2 at% Zn and 7.9 ± 2.0 at% Nd, Fig. 4(b); and the crystal structure could be indexed according the C centred orthorhombic phase, Fig. 4(c)–(e) (lattice parameters a=0.97 nm, b=1.12 nm and c=0.95 nm) reported by Huang et al. [21]. Only this phase was detected in the ZK40-2Nd alloy and it is addressed as $Mg_{75}Zn_{20}Nd_5$.

All three DTA curves show an exothermic peak, during cooling from 700 °C, at 636–638 °C attributed to the formation of α-Mg, Fig. 3(b), (d), and (f). In addition, a single peak was observed at 337.7 °C for ZK40 during cooling and the intermetallic phase formation was observed at 496.4 °C for the ZK40-2Gd. This indicated that ZK40-2Gd contained an intermetallic phase different from ZK40. In case of ZK40-2Nd two exothermic peaks were measured, at 487.8 and 466.3 °C. Based on the TEM and the SRD results only one intermetallic phase was observed in the microstructure, denoted as $Mg_{75}Zn_{20}Nd_5$ [21]. This suggests a possible transformation of the intermetallic phase during cooling. A conclusive evaluation of this is beyond the scope of this publication and this will be investigated in a later publication.

The potential differences between constituents of the different materials were investigated using SKPFM [22]. Surface potential maps and potential profiles are shown in Fig. 5 for the ZK40 (Fig. 5(a)), ZK40-2Gd (Fig. 5(b)) and ZK40-2Nd (Fig. 5(c)). Fig. 6 illustrates the surface potential maps, potential profiles and chemical composition for the impurities particles found in the ZK40-2Gd alloy (Fig. 6(a)) and for the ZK40-2Nd alloy (Fig. 6(b)). Mg-Zn-Zr-Fe impurities are cathodic with respect to the α-Mg matrix (430 ± 50 mV for the ZK40-2Gd alloy and 140 ± 30 mV for the ZK40-2Nd alloy), suggesting the formation of

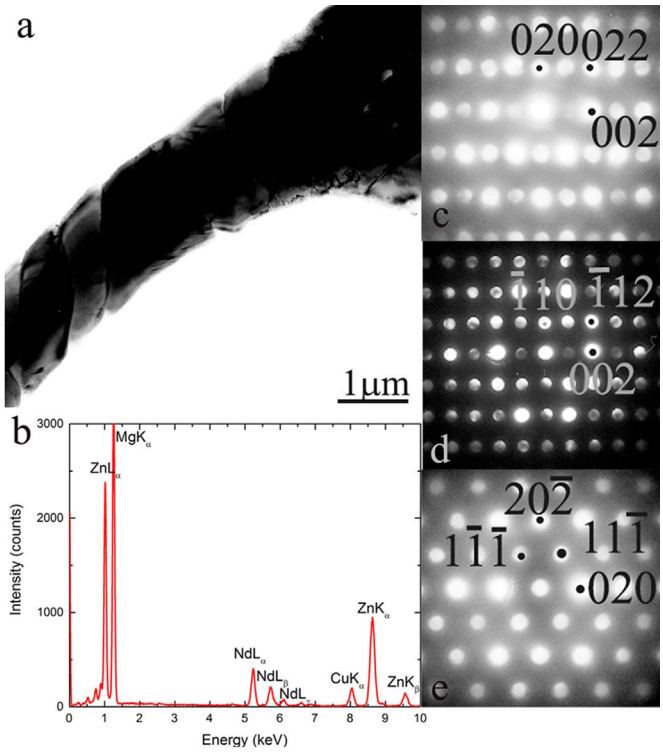

Fig. 4. TEM analyses for the ZK40-2Nd alloy: (a) the bright field image of the intermetallic phase; (b) EDS line profile for the intermetallic phase; (c)–(e) diffraction patterns for the (001), (101) and (110) zones axis, respectively.

micro-galvanic couples. The intermetallic phases present in the studied alloys were also cathodic with respect to the α-Mg matrix. For the ZK40, ZK40-2Gd and ZK40-2Nd alloys the potential difference between the intermetallic phases and the α-Mg matrix was 50 ± 20 mV, 170 ± 20 mV and 35 ± 10 mV, respectively.

3.2. Room temperature tensile and compression properties

The tensile and compression curves of the investigated alloys are shown in Fig. 7 with pertinent points summarised in Table 2. The ZK40-2Gd has the largest elongation to failure. The tensile tests show improved yield strength and the maximum tensile strength for the Gd modified alloy. The strong bonding between the intermetallic phase and the matrix can be a reason for the enhanced strength of ZK40-2Gd alloy. This effect was reported by Yu et al. [16] for a high strain-rate rolled Mg-5.5Zn-0.6Zr-xGd (x=0.2, 0.5 and 0.8 wt%). The yield strength and maximum tensile strength were significantly reduced by the Nd addition. There was no significant difference between compressive and tensile yield strengths of all three alloys. The maximum compressive strength and compression to failure did not show significant deviations from each alloy. However, the ultimate tensile stress (UTS) of ZK40-2Nd is significant smaller than other two alloys and did not show similar amount of work hardening. The elongation to failure was also significantly lower for ZK40-2Nd.

3.3. Corrosion behaviour

Based on the corrosion results, findings reveal that the corrosion resistance in NaCl aqueous solution of ZK40 alloy increases with the addition of Gd and decreases with the incorporation of Nd.

Fig. 8 shows the hydrogen evolution volume up to 7 days (for ZK40-2Nd) and 14 days (for ZK40-2Gd and ZK40) of immersion in 0.5 wt%. NaCl. The ZK40-2Nd alloy shows a considerably higher hydrogen evolution volume compared with the ZK40 and ZK40-2Gd alloys. After one day, the hydrogen evolution volume of ZK40-2Nd was 1.07 ± 0.15 ml/cm^2, whereas ZK40 alloy had produced only 0.23 ± 0.01 ml/cm^2 and the ZK40-2Gd alloy had produced 0.10 ± 0.01 ml/cm^2 of H_2. Therefore, the amount of H_2 produced by ZK40-2Nd was 5 times higher compared to the ZK40 and approximately 10 times higher than ZK40-2Gd. In the case of ZK40-2Nd alloy, the hydrogen release was very fast so that the test was interrupted after 7 days. For all immersion times, the alloy ZK40-2Gd showed the lowest hydrogen evolution values indicating the enhanced corrosion behaviour.

Hydrogen evolution results show a different tendency for short and long immersion times. At the initial stage of corrosion, an incubation period with a low rate of hydrogen evolution is observed followed by a period of acceleration in hydrogen evolution after approximately 10 h for the ZK40-2Nd alloy, 25 h for the ZK40 and 50 h for the ZK40-2Gd alloy. After approximately 150 h for the ZK40-2Gd and 175 h for the ZK40 alloy the hydrogen evolution volume reached an apparent constant increase rate, indicated by the linearity of curves of these alloys. The ZK40-2Nd alloy did not show such behaviour in the range investigated. These differences might be related with the corrosion layer formed on the surface of the different alloys [28]. After immersion in an aqueous solution, the film of MgO that formed in air will transform into a film consisting mainly of $Mg(OH)_2$. The volume expansion from MgO to $Mg(OH)_2$ is attributed as the main disruption of the surface film [29] and could explain the porous microstructure of the $Mg(OH)_2$ layer in the surface film. The initial incubation period observed during hydrogen evolution attributes to the breakdown of the MgO surface film originating cracks on the corrosion film [28]. However, once the film starts breaking down and corrosion is initiated in a specific area (localised corrosion), repairing of the corrosion film is relatively difficult. Although the dissolved Mg^{2+} can react with OH^- and deposit $Mg(OH)_2$ on the Mg surface, the loosely deposited $Mg(OH)_2$ film does not necessarily cover the cracks. Simultaneously, the hydrogen bubbles generated in the corroding areas can cause localised disruptions to the deposited $Mg(OH)_2$ preventing the corroding areas from being fully covered by the $Mg(OH)_2$. The accelerated period of hydrogen evolution is attributed to the intensive localised corrosion activity. Finally, due to the increase of the pH (intrinsically related to the redox reactions of Mg, which produce OH^- as one of the products), and taking into account that the magnesium corrosion products are stable at high pH [30], the corrosion front stabilise, leading to a nearly linear hydrogen volume increase.

EIS is an effective method to characterize metal corrosion behaviour [23,24]. Fig. 9 shows Nyquist and Bode diagrams of the EIS experimental data for the alloys after 24 h of immersion in 0.5 wt% NaCl solution. The Nyquist diagrams show a capacitive loop at high and intermediate frequencies (HF and MF), which can be attributed to the electrochemical activities in the interface metal/electrolyte (charge transfer resistance and double layer capacitance). The inductive response observed at low frequencies, is mainly related to the instability of the system and to simplify was not included in the fitting.

Based on that, a Randles equivalent circuit [25] was used to fit the EIS experimental data (insert Fig. 9(d) in the example of the fitting of the experimental data for ZK40 alloy). The circuit shows the uncompensated solution resistance (R_{el}), the time constant related to the corrosion process that can be described by the double layer capacitance on the electrolyte/metal interface (Constant Phase Element – CPEdl) and the charge transfer resistance (Rct). Constant Phase Element (CPE) was used instead of capacitances in order to account the non-ideal behaviour of the system [26]. The corresponding electrochemical parameters are presented in Table 3.

R_{el} values were comparable for all the alloys and were in the range between 85 and 100 Ω cm^2. The diameter of the capacitive loop observed in the Nyquist diagram (Fig. 9(a)) of the ZK40-2Gd alloy reaches Z' values around 1100 Ω cm^2, which is higher than that of the ZK40 alloy (700 Ω cm^2), and significantly higher than the ZK40-2Nd alloy (400 Ω cm^2), indicating a higher corrosion resistance of the ZK40-2Gd alloy.

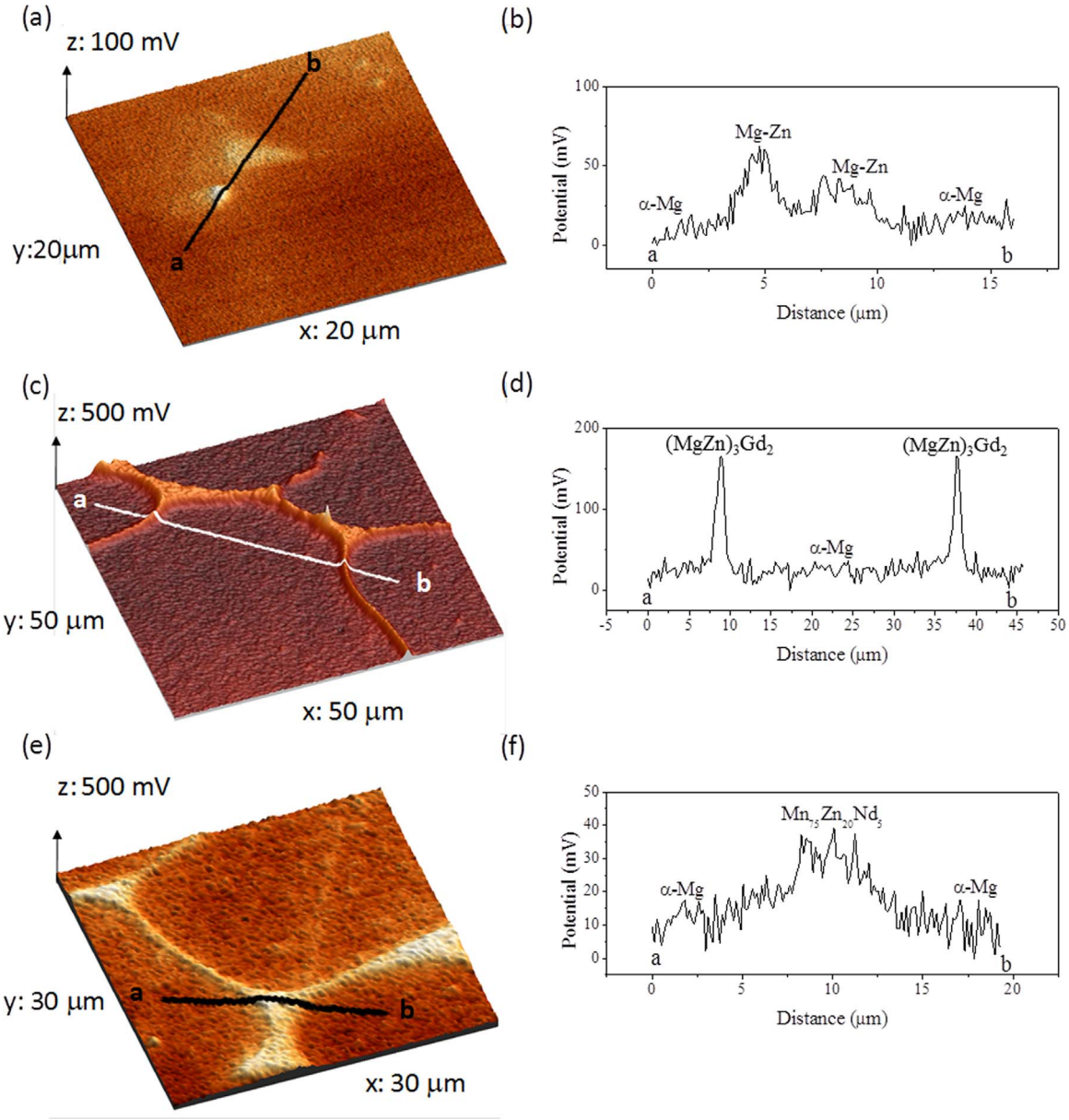

Fig. 5. Surface potential maps and potential profiles for (a), (b) KZ40, (c), (d) KZ40-2Gd and (e), (f) KZ40-2Nd alloys.

CPE-T values of the dielectric layer of ZK40-2Nd (220.0 µF cm^{-2}) after 24 h immersion are approximately 2.5 times higher than those of the ZK40 alloy (75.1 µF cm^{-2}) and the ZK40-2Gd alloy (65.6 µF cm^{-2}). This is associated with the greater active area in ZK40-2Nd alloy exposed to the electrolyte. CPE-n value is the highest for the ZK40-2Gd alloy and the smallest for the ZK40-2Nd alloy, suggesting that there is an increase in the heterogeneity of the surface due to the corrosion process in the ZK40-2Nd alloy. The calculated CPE-T values increased with time for all investigated alloys.

Higher values of the charge transfer resistance (485.5 Ω cm^2) for the ZK40-2Gd alloy, after 24 h of immersion, compared to ZK40 alloy (412.3 Ω cm^2) and ZK40-2Nd alloy (133.3 Ω cm^2) reveals its enhanced corrosion resistance. The R_{ct} decreased for all alloys with the immersion time, due to the propagation of the corrosion process as was reported by Arrabal et al. [31].

Fig. 10 shows the plan view of the corroded specimens, after the removal of the corrosion products, for immersion times of 4 h (Fig. 10(a)–(c)), 8 h (Fig. 10(d)–(f)) and 24 h (Fig. 10(g)–(i)) in 0.5 wt% NaCl solution. In all the cases, localised corrosion is observed characterised by micro "craters" in the α-Mg matrix, with about 1 µm of diameter. In the particular case of ZK40-2Nd alloy, localised corrosion along the intermetallic particles was also observed (insert of Fig. 10(c), (f)). This alloy shows the most severe corrosion attack after 24 h of immersion (Fig. 10(i)).

Mainly two factors can be discussed in terms of corrosion behaviour:

(i) Micro-galvanic effect between the α-Mg matrix and second phases and between the α-Mg matrix and the impurities: In general, this topic has been studied extensively and almost all the intermetallic phases in Mg alloys are more noble compared to the α-Mg matrix, as reported for AZ alloys [32–34], ZE41 [35,36], Mg-xGd-3Y-O.4Zr (x=6, 8, 10, 12%) [37], Mg-10Gd-3Y-0.4Zr [38], Mg-Zn-RE [39], Mg-6Zn-1Y-0.6Zr [40], Mg-Zn-Mn-Si-Ca [41,42], Mg-8Li [43] and Mg-RE (0.5–5% La, 0.5–5% Ce, 0.5–4% Nd) [44]. The SKPFM analysis (Figs. 5 and 6) indicates that for the ZK40-2Gd and ZK40-2Nd the impurities has a higher Volta potential surface potential compared with the matrix, and it is significantly higher than the potential difference between the intermetallic compounds and the matrix. However, the initial steps of corrosion (up to 24 h

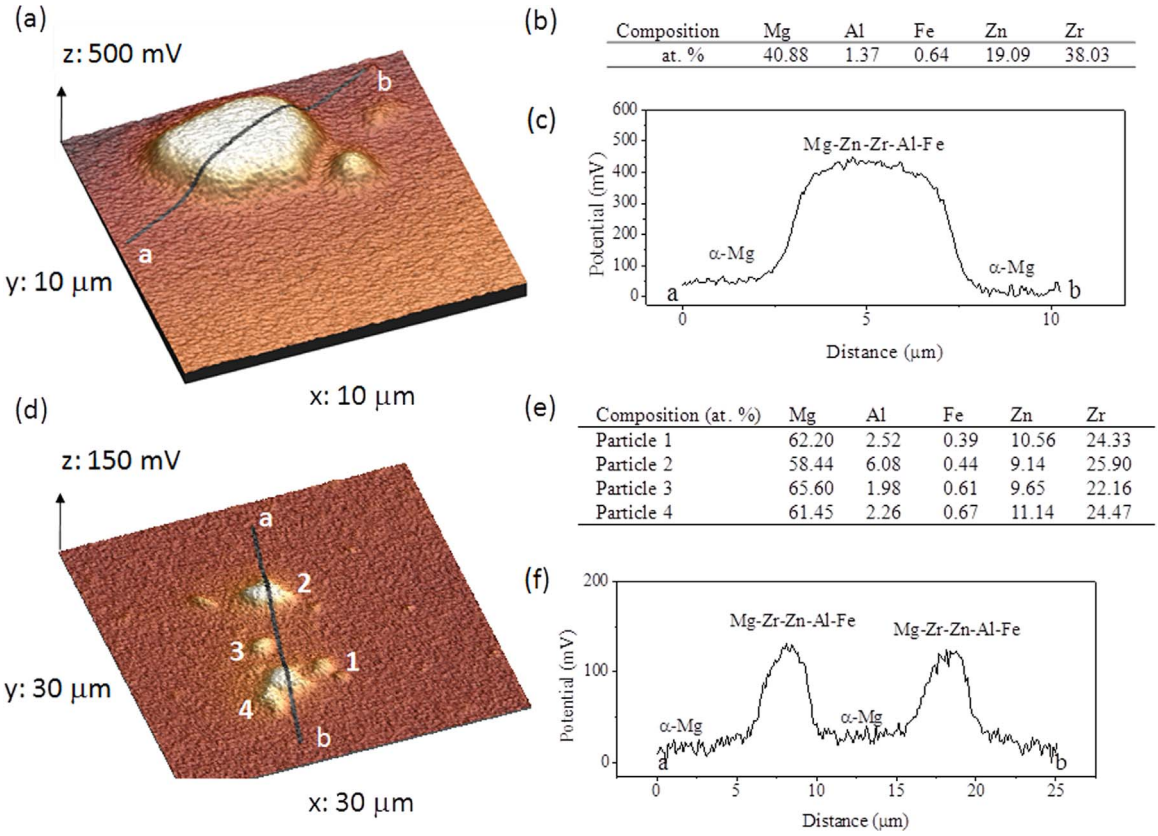

Fig. 6. Surface potential maps, composition and potential profiles in regions containing impurities for (a)–(c) KZ40-2Gd and (d)–(f) KZ40-2Nd.

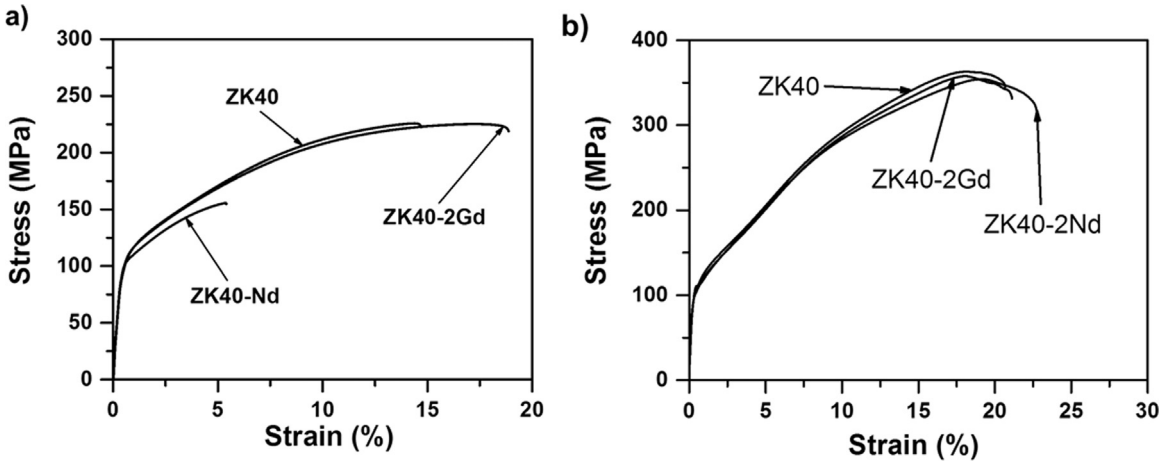

Fig. 7. Typical tensile (a) and compressive (b) nominal stress-strain curves for the ZK40, ZK40-2Gd and ZK40-2Nd alloys.

Table 2
Mechanical properties at room temperature: compression and tensile values for the ZK40 alloy, ZK40-2Gd alloy and ZK40-2Nd alloy.

	Tensile properties			Compression properties		
	Yield stress (MPa)	Maximum stress (MPa)	Elongation at failure	Yield stress (MPa)	Maximum stress (MPa)	Elongation at failure
ZK40	101.8 ± 6.7	225.1 ± 15.2	12.8 ± 4.6	106.8 ± 3.0	365.2 ± 3.6	20.6 ± 1.3
ZK40-2Gd	99.8 ± 6.1	227.9 ± 6.5	17.9 ± 1.9	107.3 ± 2.7	360.9 ± 3.8	20.2 ± 1.5
ZK40-2Nd	99.3 ± 2.7	147.5 ± 10.3	3.9 ± 1.0	109.3 ± 2.4	351.3 ± 2.3	22.3 ± 2.1

of immersion) (Fig. 10) does not show strong evidence of micro-galvanic effect due to these impurities. Thus, the impurities can act as initiation points of corrosion but did not play an important role on the development of corrosion within the α-Mg matrix. Regarding the corrosion mechanism, for the ZK40 and ZK40-2Gd alloys, the corrosion started within the grain, as illustrated by the "craters", Fig. 10(b). Additionally, "micro craters" of ~1 μm diameter are observed in the middle of the grain for all alloys, but not close to the grain boundaries in the case of the ZK40-2Gd which is in concordance with other work [10]. The different

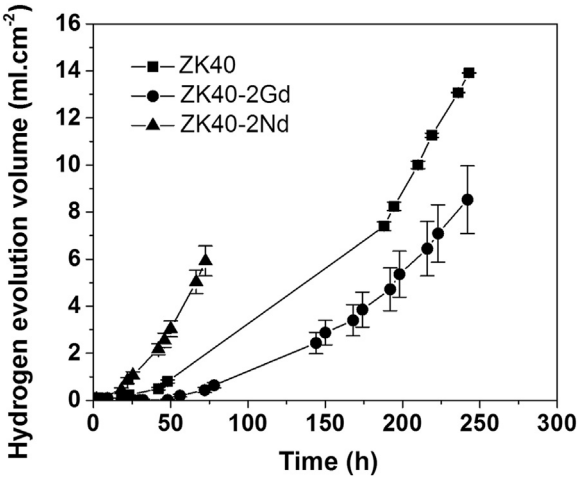

Fig. 8. Hydrogen evolution in 0.5 wt% NaCl solution for the ZK40 alloy, ZK40-2Gd alloy and ZK40-2Nd alloy.

corrosion morphology of the alloys might be related to the presence of second phases but also to the chemical segregation of the different alloying elements in the α-Mg matrix. In the case of ZK40 and ZK40-2Gd, the higher concentration of Zn near the grain boundary enhanced the corrosion resistance of this area for the ZK40 and ZK40-2Gd. The segregation of Zn is higher for the ZK40 compared with the ZK40-2Gd. The presence of high amount of Zr in the centre of the grain for the ZK40-2Gd did not seem to enhance to corrosion resistance of the α-Mg matrix. In the particular case of ZK40-2Nd alloy, localised corrosion along the

Table 3
Simulated parameters of the electrochemical impedance spectroscopy (EIS) data of the investigated ZK40, ZK40-2Gd and ZK40-2Nd alloys after 24 h.

Time (h)	R_{el} (Ω)	R_{ct} (Ω cm^2)	CPE-T (μF cm^{-2})	CPE-P
ZK40				
1	84.7 ± 0.5	702.9 ± 6.7	23.1 ± 0.7	0.880 ± 0.005
3	84.9 ± 0.5	581.2 ± 5.7	31.1 ± 1.0	0.892 ± 0.005
6	87.3 ± 0.6	525.0 ± 6.1	39.3 ± 1.6	0.893 ± 0.007
10	86.4 ± 0.5	494.6 ± 5.3	45.1 ± 1.6	0.909 ± 0.006
16	86.4 ± 0.4	452.0 ± 4.6	64.5 ± 2.1	0.877 ± 0.007
24	85.8 ± 0.4	412.3 ± 4.8	75.1 ± 2.7	0.876 ± 0.006
ZK40–2Gd				
1	84.7 ± 0.9	1131.0 ± 16.5	19.9 ± 1.0	0.868 ± 0.008
3	87.1 ± 0.5	677.5 ± 6.8	24.5 ± 0.8	0.904 ± 0.006
6	87.4 ± 0.5	627.2 ± 6.7	35.2 ± 1.2	0.905 ± 0.006
10	89.3 ± 0.5	594.3 ± 6.0	43.8 ± 1.4	0.906 ± 0.006
16	89.4 ± 0.6	458.7 ± 6.7	45.2 ± 2.1	0.927 ± 0.009
24	88.1 ± 0.4	485.5 ± 5.2	65.6 ± 3.4	0.892 ± 0.006
ZK40–2Nd				
1	94.8 ± 1.0	413.2 ± 7.7	41.6 ± 3.3	0.831 ± 0.013
3	97.3 ± 0.5	213.8 ± 2.6	45.0 ± 2.6	0.901 ± 0.010
6	96.6 ± 0.5	165.4 ± 2.2	75.1 ± 4.9	0.889 ± 0.012
10	97.7 ± 0.5	152.8 ± 1.9	117.0 ± 7.0	0.860 ± 0.011
16	100.0 ± 0.5	150.9 ± 2.3	164.0 ± 10.6	0.840 ± 0.013
24	100.1 ± 0.5	133.3 ± 2.4	220.0 ± 15.7	0.824 ± 0.014

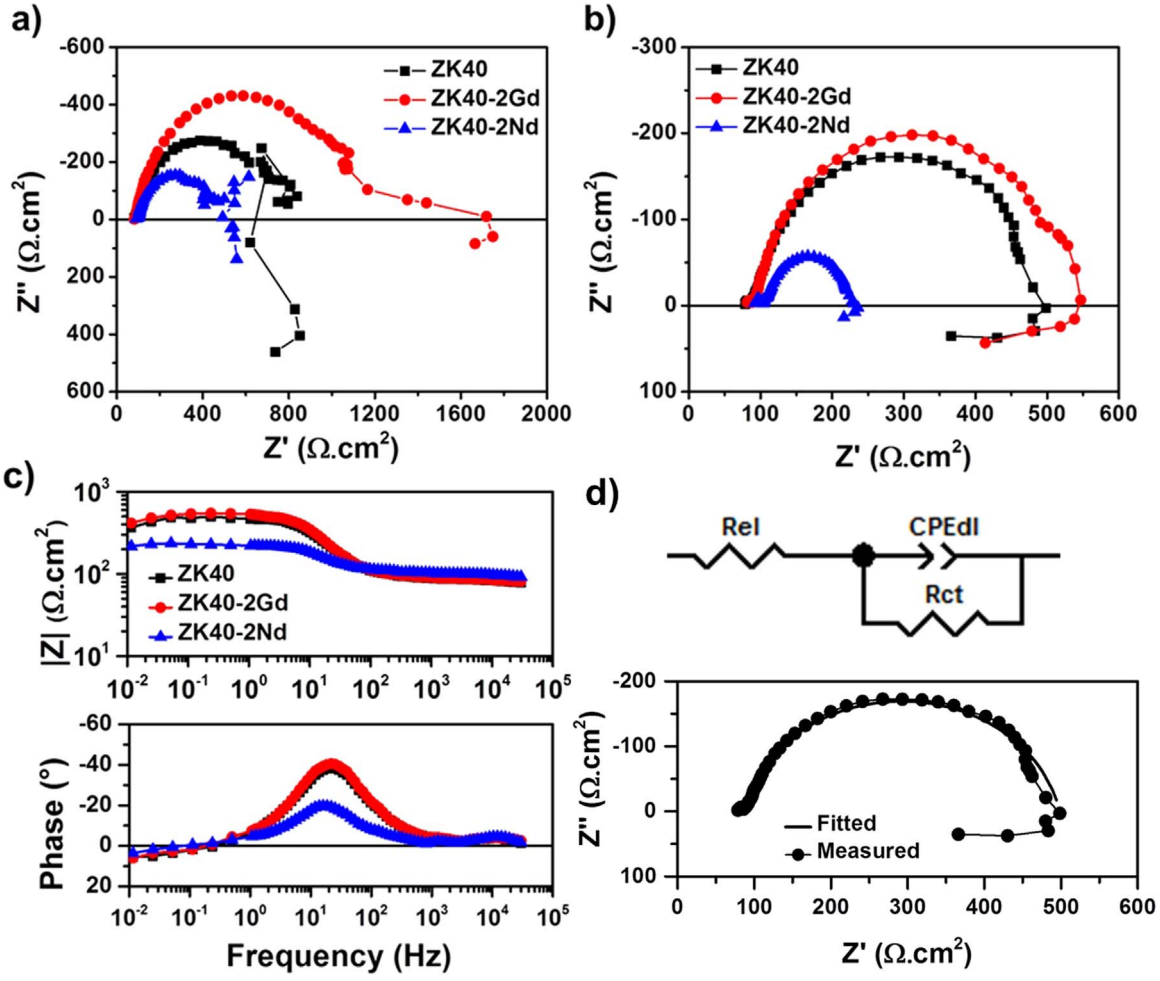

Fig. 9. Nyquist diagrams obtained by EIS in 0.5 wt% NaCl solution after (a) 1 h; (b) 24 h; (c) Bode plots obtained by EIS in 0.5 wt% NaCl solution after 24 h; (d) measured and calculated Nyquist diagrams for the ZK40 alloy from EIS in 0.5 wt% NaCl solution after 24 h as well as the equivalent circuit for EIS analysis.

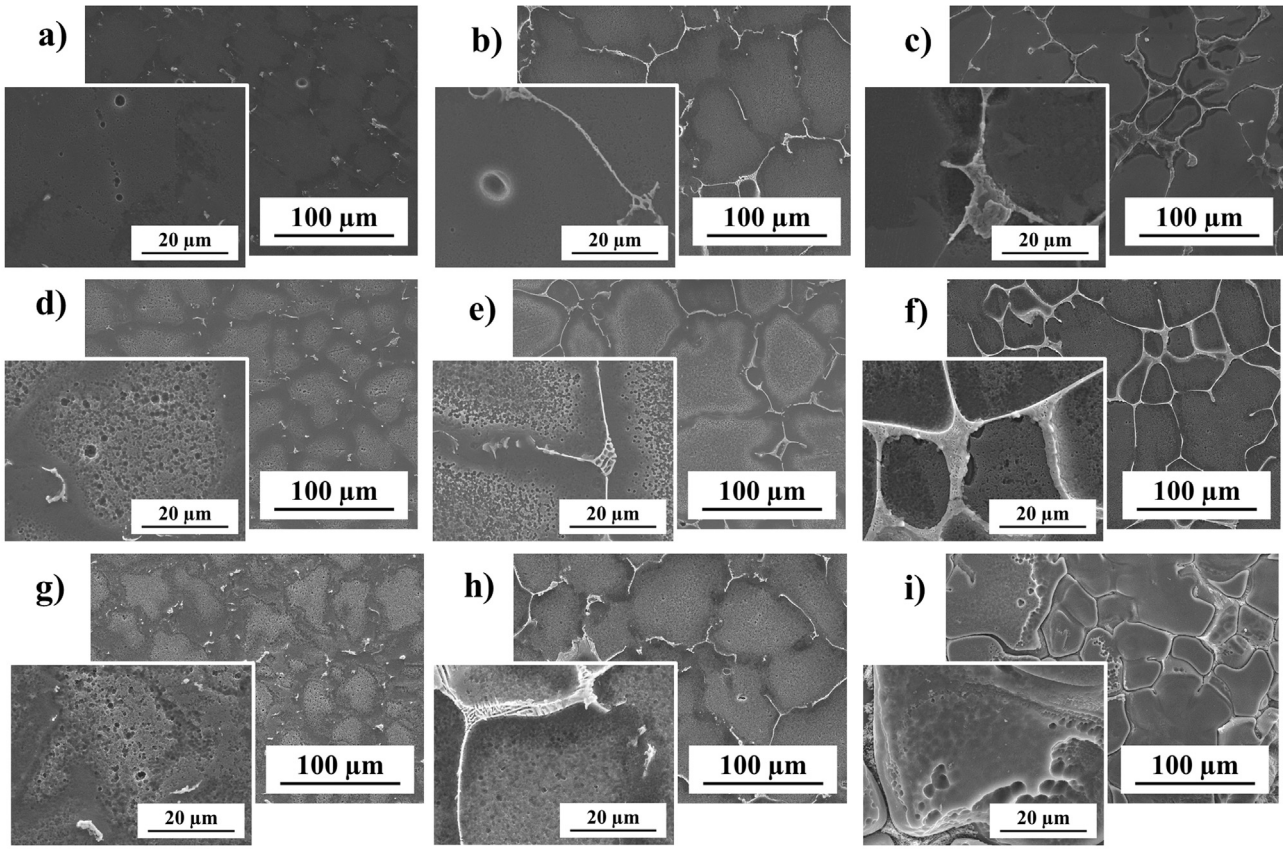

Fig. 10. First steps corrosion SE pictures after 4 h (a), (d), (g), 8 h (b), (e), (h) and 24 h (c), (f), (i) in 0.5 wt% NaCl for the ZK40 alloy (a)–(c), ZK40-2Gd (d)–(f) and ZK40-2Nd alloy (g)–(i).

intermetallic compounds also play a role (Fig. 10(c), (f), and (i)) on the corrosion mechanism. This effect was not observed for the ZK40 or the ZK40-2Gd. This result is unexpected as the SKPFM results for ZK40-2Nd alloy show that the Volta potential difference between the α-Mg matrix and the intermetallic compound was not large. The SKPFM measures the surface potential difference. It is expected that the highest the potential difference between the two surfaces results in a higher microgalvanic couple. The presence of microgalvanic couples can lead to microgalvanic corrosion. For the ZK40-2Nd, the localised corrosion of the α-Mg matrix along the intermetallic phase suggests that not only the nobility of the intermetallic phase played an important role during immersion in 0.5 wt% NaCl but other mechanisms of corrosion also contributes to the corrosion process. The chemical segregation for the ZK40-2Nd alloy was nearly absence. For the ZK40 and ZK40-2Gd alloys the grain boundary could act as cathodic areas related to the α-Mg matrix, prevent the grain boundaries to corrode. The absence of this effect for the ZK40-2Nd alloy could have enhanced the corrosion of the α-Mg matrix along the intermetallic compound;

(ii) The barrier effect of second phases: As reported for AZ series magnesium alloys [45,46], the barrier effect due to the presence of a semi continuous network of intermetallic particles along the grain boundaries can prevent the advance corrosion front into the α-Mg matrix. However, the intermetallic particles along the grain boundary in ZE41 alloy did not behave as a barrier for the advance of corrosion [9]. Similar features were found in this work for the ZK40-2Nd alloy, without an important contribution of the second phase acting as a barrier. For the ZK40-2Gd the absence of localised corrosion along the grain boundary might have promoted the "barrier effect" of the semi continuous of $(Mg, Zn)_3Gd_2$ intermetallic compound.

4. Conclusions

The addition of Gd and Nd modified the as-cast microstructure of the ZK40 alloy. There is no significant change in the yield and ultimate strengths with addition of Gd to ZK40 but elongation until fracture in tension increased with Gd addition. The corrosion resistance measured by impedance and hydrogen evolution was slightly enhanced for the ZK40-2Gd and very poor corrosion resistance was exhibited for the ZK40-2Nd. A complex series of localised corrosion at various microstructures features can explain the different corrosion behaviour:

(1) Mg-Zn-Zr-Al-Fe impurities did not play an important role on corrosion;
(2) The morphology of localised corrosion of the different alloys is associated to the presence of secondary phases and the chemical segregation for the different alloying elements in the α-Mg matrix;
(3) Severe localised corrosion along the intermetallic particles along the grain boundaries was observed for the ZK40-2Nd alloy. The corrosion front propagated faster for this alloy.

The enhanced mechanical and corrosion properties observed in ZK40-2Gd alloy make the Mg-Zn-Zr-Gd an interesting magnesium alloy with for further development with a view for structural applications.

Acknowledgements

The authors acknowledge the *Deutsches Elektronen-Synchrotron* (DESY) for the provision of facilities within the framework of proposal I-20130434. RHB acknowledges University of Sao Paulo for granting the fellowship *´Bolsa Empreendedorismo´*. MM acknowledges the Alexander von Humboldt foundation for the provision of financial

support in the form of post-doctoral fellowship.

References

[1] K.U. Kainer, Magnesium Alloys and Technology, Wiley-VCH, Weiheim, 2003.
[2] A.A. Luo, Wrought magnesium alloys and manufacturing processes for automotive applications, SAE Trans. 114.5 (2005) 411–421.
[3] J. Zhang, J. Wang, X. Qiu, D. Zhang, Z. Tian, X. Niu, D. Tang, J. Meng, Effect of Nd on the microstructure, mechanical properties and corrosion behavior of die-cast Mg–4Al-based alloy, J. Alloy. Compd. 464.1 (2008) 556–564.
[4] T. Zhang, G. Meng, Y. Shao, Z. Cui, F. Wang, Corrosion of hot extrusion AZ91 magnesium alloy. Part II: effect of rare earth element neodymium (Nd) on the corrosion behavior of extruded alloy, Corros. Sci. 53 (2011) 2934–2942.
[5] G. Wu, Y. Fan, H. Gao, C. Zhai, Y.P. Zhu, The effect of Ca and rare earth elements on the microstructure, mechanical properties and corrosion behavior of AZ91D, Mater. Sci. Eng. A 408 (2005) 255–263.
[6] R. Ambat, N.N. Aung, W. Zhou, Evaluation of microstructural effects on corrosion behaviour of AZ91D magnesium alloy, Corros. Sci. 42.8 (2000) 1433–1455.
[7] O. Lunder, M. Videm, K. Nisancioglu, Corrosion resistant magnesium alloys, SAE Tech. Pap. (1995) 950428.
[8] M. Yamasaki, N. Hayashi, S. Izumi, Y. Kawamura, Corrosion behavior of rapidly solidified Mg–Zn–rare earth element alloys in NaCl solution, Corros. Sci. 49.1 (2007) 255–262.
[9] M.C. Zhao, M. Liu, G.L. Song, A. Atrens, Influence of microstructure on corrosion of As-cast ZE41, Adv. Eng. Mater. 10 (1–2) (2008) 104–111.
[10] W.C. Neil, M. Forsyth, P.C. Howlett, C.R. Hutchinson, B.R.W. Hinton, Corrosion of magnesium alloy ZE41–The role of microstructural features, Corros. Sci. 51.2 (2009) 387–394.
[11] C. Ma, M. Liu, G. Wu, W. Ding, Y. Zhu, Tensile properties of extruded ZK60–RE alloys, Mater. Sci. Eng. A 349.1 (2003) 207–212.
[12] T.E. Leontis, Magnesium and magnesium alloys-the room and elevated temperature properties of some sand cast magnesium-base alloys containing zinc, Trans. AIME 185 (1949) 327.
[13] Q. Li, Q. Wang, Y. Wang, X. Zeng, W. Ding, Effect of Nd and Y addition on microstructure and mechanical properties of as-cast Mg–Zn–Zr alloy, J. Alloy. Compd. 427.1 (2007) 115–123.
[14] Y.A.N.G. Mingbo, G.U.O. Tingzhang, Q.I.N. Caiyuan, P.A.N. Fusheng, Microstructure, tensile and creep properties of as-cast Mg-3.8 Zn-2.2 Ca-xCe (x=0, 0.5, 1 and 2 wt%) magnesium alloys, J. Rare Earths 30.2 (2012) 181–188.
[15] N. Stanford, D. Atwell, M.R. Barnett, The effect of Gd on the recrystallisation, texture and deformation behaviour of magnesium-based alloys, Acta Mater. 58.20 (2010) 6773–6783.
[16] H. Yu, Y. Hongge, C. Jihua, S. Bin, Z. Yi, S. Yanjin, M. Zhaojie, Effects of minor Gd addition on microstructures and mechanical properties of the high strain-rate rolled Mg–Zn–Zr alloys, J. Alloy. Compd. 586 (2014) 757–765.
[17] M.M. Avedesian, H. Baker, Magnesium and Magnesium Alloys, ASM Speciality Handbook, ASM International, United States of America, 1999.
[18] J. Luo, K. Ying, P. He, J. Bai, Properties of Savitzky–Golay digital differentiators, Digit. Signal Process. 15.2 (2005) 122–136.
[19] G. Song, A. Atrens, Understanding magnesium corrosion—a framework for improved alloy performance, Adv. Eng. Mater. 5.12 (2003) 837.
[20] G. Song, A. Atrens, D. StJohn, An hydrogen evolution method for the estimation of the corrosion rate of magnesium alloys, Magnes. Technol. 2001 (2001) 254–262.
[21] M.L. Huang, H.X. Li, H. Ding, Z.Y. Tang, R.B. Mei, H.T. Zhou, R.P. Ren, S.M. Hao, A ternary linear compound T 2 and its phase equilibrium relationships in Mg–Zn–Nd system at 400 °C, J. Alloy. Compd. 489.2 (2010) 620–625.
[22] M. Nonnenmacher, M.P. o'Boyle, H.K. Wickramasinghe, Kelvin probe force microscopy, Appl. Phys. Lett. 58.25 (1991) 2921–2923.
[23] N. Pebere, C. Riera, F. Dabosi, Investigation of magnesium corrosion in aerated sodium sulfate solution by electrochemical impedance spectroscopy, Electrochim. Acta 35 (1990) 555–561.
[24] C.B.G. Baril, N. Pebere, AC impedance spectroscopy in characterizing time-dependent corrosion of AZ91 and AM50 magnesium alloys characterization with respect to their microstructures, J. Electrochem. Soc. 148 (2001) B489–B496.
[25] K. Hladky, L.M. Callow, J.L. Dawson, Corrosion rates from impedance measurements: an introduction, Br. Corros. J. 15.1 (1980) 20–25.
[26] G.J. Brug, A.L.G. Van Den Eeden, M. Sluyters-Rehbach, J.H. Sluyters, The analysis of electrode impedances complicated by the presence of a constant phase element, J. Electroanal. Chem. Interfacial Electrochem. 176.1 (1984) 275–295.
[27] S.J. Liu, G.Y. Yang, S.F. Luo, W.Q. Jie, Microstructure and mechanical properties of sand mold cast Mg–4.58 Zn–2.6 Gd–0.18 Zr magnesium alloy after different heat treatments, J. Alloy. Compd. 644 (2015) 846–853.
[28] G.-L. Song, Corrosion of Magnesium Alloys, Woodhead Publishing, Oxford, 2011.
[29] H.B. Yao, Y. Li, A.T.S. Wee, An XPS investigation of the oxidation/corrosion of melt-spun Mg, Appl. Surf. Sci. 158 (2000) 112–119.
[30] J.H. Nordlien, S. Ono, N. Masuko, K. Nisancioglu, A. TEM, Investigation of naturally formed oxide films on pure magnesium, Corros. Sci. 39.8 (1997) 1397–1414.
[31] R. Arrabal, A. Pardo, M.C. Merino, M. Mohedano, P. Casajús, K. Paucar, G. Garcés, Effect of Nd on the corrosion behaviour of AM50 and AZ91D magnesium alloys in 3.5 wt% NaCl solution, Corros. Sci. 55 (2012) 301–312.
[32] G.-L. Song, A. Atrens, M. Dargusch, Influence of microstructure on the corrosion of diecast AZ91D, Corros. Sci. 41 (1999) 249–273.
[33] M.C. Zhao, M. Liu, G. Song, A. Atrens, Influence of the β-phase morphology on the corrosion of the Mg alloy AZ91, Corros. Sci. 50 (2008) 1939.
[34] M.C. Zhao, M. Liu, G. Song, A. Atrens, Influence of homogenization annealing of AZ91 on mechanical properties and corrosion behaviour, Adv. Eng. Mater. 10 (2008) 93–103.
[35] M.C. Zhao, M. Liu, G. Song, A. Atrens, Influence of microstructure on corrosion of As-cast ZE41, Adv. Eng. Mater. 10 (2008) 104–111.
[36] M.C. Zhao, M. Liu, G.-L. Song, A. Atrens, Influence of pH and chloride ion concentration on the corrosion of Mg alloy ZE41, Corros. Sci. 50 (2008) 3168–3178.
[37] J. Chang, X. Guo, S. He, P. Fu, L. Peng, W. Ding, Investigation of the corrosion for Mg–xGd–3Y–0.4 Zr (x=6, 8, 10, 12 wt%) alloys in a peak-aged condition, Corros. Sci. 50 (2008) 166–177.
[38] L.M. Peng, J.W. Chang, X.W. Guo, A. Atrens, W.J. Ding, Y.H. Peng, Influence of heat treatment and microstructure on the corrosion of magnesium alloy Mg-10Gd-3Y-0.4 Zr, J. Appl. Electrochem. 39 (2009) 913–920.
[39] M. Yamasaki, N. Hayashi, S. Izumi, Y. Kawamura, Corrosion behavior of rapidly solidified Mg–Zn–rare earth element alloys in NaCl solution, Corros. Sci. 49 (2007) 255–262.
[40] Y. Song, D. Shan, R. Chen, E.H. Han, Effect of second phases on the corrosion behaviour of wrought Mg–Zn–Y–Zr alloy, Corros. Sci. 52 (2010) 1830–1837.
[41] Y. Lisitsyn, G. Ben-Hamu, D. Eliezer, K.S. Shin, Some particularities of the corrosion behaviour of Mg–Zn–Mn–Si–Ca alloys in alkaline chloride solutions, Corros. Sci. 52 (2010) 2280–2290.
[42] Y. Lisitsyn, G. Ben-Hamu, D. Eliezer, K.S. Shin, The role of Ca microalloying on the microstructure and corrosion behavior of Mg–6Zn–Mn–(0.5–2) Si alloys, Corros. Sci. 51 (2009) 776–784.
[43] Y. Song, D. Shan, R. Chen, E.H. Han, Corrosion characterization of Mg–8Li alloy in NaCl solution, Corros. Sci. 51 (2009) 1087–1094.
[44] N. Birbilis, M.A. Easton, A.D. Sudholz, S.M. Zhu, M.A. Gibson, On the corrosion of binary magnesium-rare earth alloys, Corros. Sci. 51 (2009) 683.
[45] A.E. Coy, F. Viejo, P. Skeldon, G.E. Thompson, Susceptibility of rare-earth-magnesium alloys to micro-galvanic corrosion, Corros. Sci. 52.12 (2010) 3896–3906.
[46] I. Apachitei, L.E. Fratila-Apachitei, J. Duszczyk, Microgalvanic activity of an Mg–Al–Ca-based alloy studied by scanning Kelvin probe force microscopy, Scr. Mater. 57.11 (2007) 1012–1015.